Evolution of short-range order in chemically and physically grown thin film bilayer structures for electronic applications

Ann-Christin Dippel, Olof Gutowski, Lars Klemeyer, Ulrich Boettger, Fenja Berg, Theodor Schneller, Alexander Hardtdegen, Stephan Aussen, Susanne Hoffmann-Eifert, and Martin v. Zimmermann

Electronic supplementary information

Content

Section S1:
Details on the particular challenges in HfO_2 based resistive switching devices and on the development of optimised devices

Section S2 (Tables S1-2 and Figures S1-7):
Results from the film characterisation by x-ray reflectometry (XRR)

Section S3 (Table S3 and Figures S8-11):
Supplementary information for the PDF analysis of sample type (i) PZT on Pt

Section S4 (Tables S4-7 and Figures S12-16):
Supplementary information for the PDF analysis of sample type (ii) HfO_2 on TiN and sample type (iii) TiO_x on HfO_2

Section S1: Details on the particular challenges in HfO_2 based resistive switching devices and on the development of optimised devices

Generally, after an initial electroforming step, HfO_2-based ReRAM devices reveal filamentary-type bipolar switching of the resistance state between high and low values (ON and OFF states) triggered by voltage application (SET and RESET). The commonly accepted physical model considers a valance change of the transition metal ions, resulting from the creation, annihilation, drift and diffusion processes of oxygen vacancy defects. Therefore, controlling of the type and concentration of defects in the switching oxide material by means of process control and device design is of utmost importance. A challenge of memristive devices from a single layer of HfO_2 arises from considerable variations in the high resistance states and SET voltages from cycle-to-cycle. This high variability can lead to severe issues regarding read and write failures of the ReRAM devices. Hardtdegen et al. (ref. 34 in the main article) demonstrated that a bilayer structure with a thin TiO_x interlayer added between the HfO_2 resistive switching layer and the oxygen exchange metal (here Ti) significantly improves the memristive performance. The layer stack of the electrical devices is built of a Pt bottom electrode, 3 nm HfO_2 by plasma assisted ALD, 3 nm TiO_x by thermal ALD, 10 nm Ti oxygen exchange layer, and a Pt top electrode.

Studies of the ALD growth processes of HfO_2 and TiO_x revealed a linear change in thickness with increasing number of deposition cycles. In addition, under the process conditions chosen for HfO_2 and TiO_x, no change of the amorphous layer structure nor the films' low roughness values were observed for layer thicknesses increased from 3 nm to 50 nm. In order to enhance the signal for the total scattering experiments, the bilayer samples were thus fabricated from 30 nm TiO_x on top of 35-40 nm HfO_2 deposited on the fused silica substrate.

Section S2: Results from the film 3haracterization by x-ray reflectometry (XRR)

(I) HfO_2 and TiN grown by reactive sputtering

(discussed in section '3.2 HfO_2 on TiN for ReRAM applications', respective PDFs shown in Fig. 3 of the main article)

The layer stack which was utilised for the fitting is given as follows from bottom to top: fused sililca (SiO_2) as substrate with TiN and HfO_2 layers deposited by reactive sputtering. Table S1 gives a summary of the fitting results for the layers of this study. Figures S1 and S2 show the measured XRR data (black circles) and the fits (red lines).

Table S1: Properties of the sputter deposited HfO_2 on TiN layer stacks

sample description	XRR fitting			
	material	thickness / nm	roughness / nm	density / g/cm^3
HfO_2 as-deposited	HfO_2	18.4	1.4	9.8
	TiN	39.5	1.1	4.7
HfO_2 post-annealed	HfO_2	17.7	1.4	9.8
	TiN	36.9	1.0	4.8

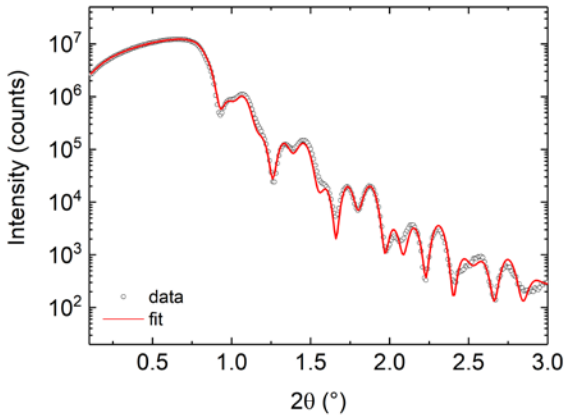

material	thickness [nm]	density [atoms/Å^3]	roughness [nm]
HfO_2	18.4	0.028	1.4
TiN	39.5	0.046	1.1
SiO_2 (fused silica)	0	0.023	0.4

Figure S1: XRR measurement and fit of the stack fused silica/TiN/HfO_2 (as-deposited).

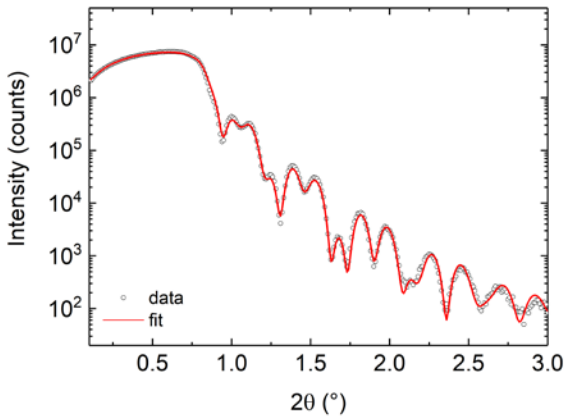

material	thickness [nm]	density [atoms/Å^3]	roughness [nm]
HfO_2	17.7	0.028	1.4
TiN	36.9	0.047	1.0
SiO_2 (fused silica)	0	0.023	0.4

Figure S2: XRR measurement and fit of the stack fused silica/TiN/HfO_2 (post-annealed).

(II) TiO_x and HfO_2 grown by atomic layer deposition (ALD).

(discussed in section '3.3 TiO_x on HfO_2 for ReRAM applications', respective PDFs shown in Figures 4 and 5 of the main article)

The analyses were performed on reference layers which were grown in the same run with the PDF samples, but on an oxidized silicon wafer instead of the fused silica substrate.

The layer stack which was utilised for the fitting is given as follows from bottom to top: silicon wafer with a thin layer of native SiO_2 and the layer or layer stack grown by ALD. Table S2 gives a summary of the fitting results for the layers of this study. Figures S3-S7 show the measured XRR data (black circles) and the fits (red lines).

Table S2: Properties of the ALD grown TiO_x and HfO_2 layers and stacks

sample description	XRR fitting			
	material	thickness / nm	roughness / nm	density / g/cm^3
85 nm TiO_x	TiO_2	83.5	1.2	3.97
30 nm TiO_x	TiO_2	28.4	1.2	3.97
30 nm TiO_x on HfO_2	TiO_2	29.7	1.3	3.97
	HfO_2	37.9	0.7	8.74
HfO_2 200 °C	HfO_2	39.1	1.0	8.91
HfO_2 300 °C	HfO_2	34.9	1.0	9.44

For the thermal TiO_x process and the plasma HfO_2 processes at 200 °C and 300 °C, growth per cycle values of (0.040 ± 0.006) nm, (1.10 ± 0.03) nm, and (1.00 ± 0.03) nm were determined, respectively. The increase in growth rate of the HfO_2 films at lower temperature is attributed to approaching the limit of the ALD HfO_2 process window towards low temperatures.

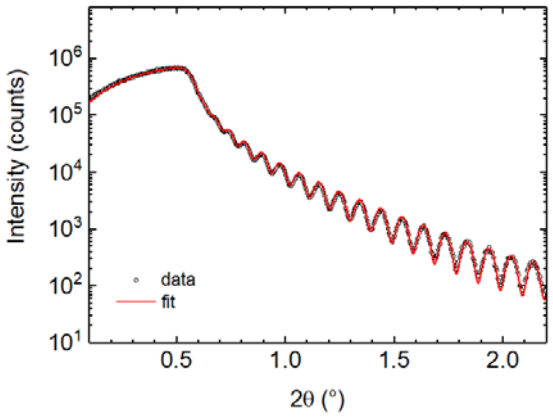

material	thickness [nm]	density [atoms/Å^3]	roughness [nm]
TiO_2	83.5	0.029	1.2
SiO_2 (native oxide)	1.9	0.023	0.24
Si	0	0.050	0.55

Figure S3: XRR measurement and fit of Si/native SiO_2/ 83.5 nm TiO_x by thermal ALD.

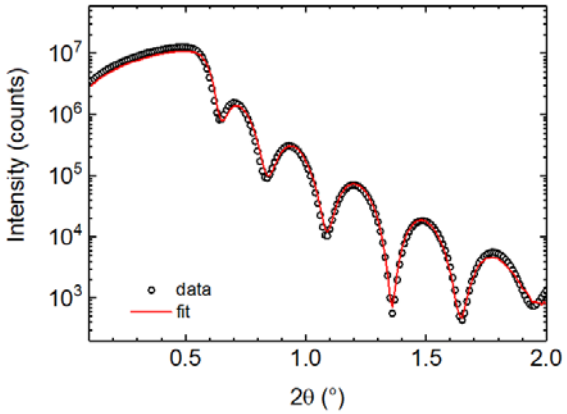

material	thickness [nm]	density [atoms/Å^3]	roughness [nm]
TiO_2	28.4	0.029	1.2
SiO_2 (native oxide)	1.9	0.023	0.24
Si	0	0.050	0.55

Figure S4: XRR measurement and fit of Si/native SiO_2/ 28.4 nm TiO_x by thermal ALD.

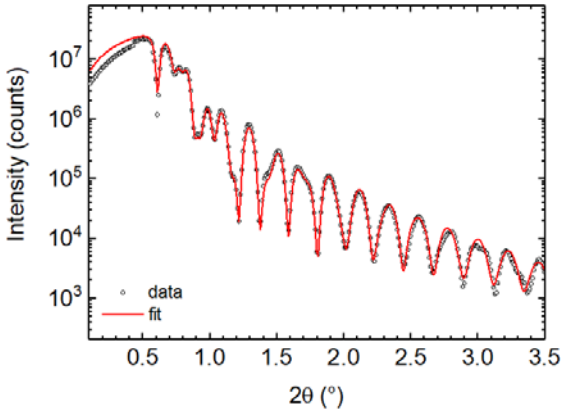

material	thickness [nm]	density [atoms/Å^3]	roughness [nm]
TiO_2	29.7	0.029	1.3
HfO_2	37.9	0.025	0.7
SiO_2 (native oxide)	1.9	0.023	0.24
Si	0	0.050	0.55

Figure S5: XRR measurement and fit of Si/native SiO_2/ 37.9 nm HfO_2 (plasma-assisted ALD, 200 °C) / 29.7 nm TiO_x (thermal ALD).

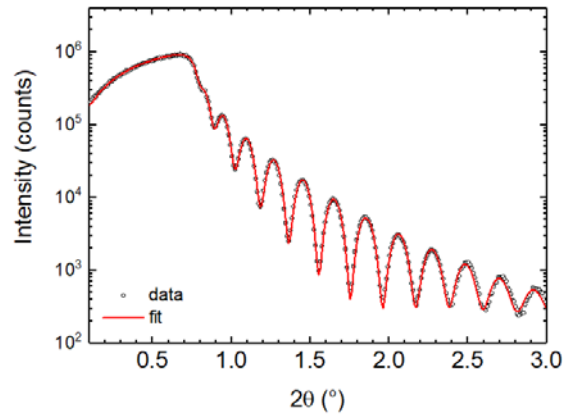

material	thickness [nm]	density [atoms/Å^3]	roughness [nm]
HfO_2	39.1	0.025	1.0
SiO_2 (native oxide)	1.9	0.023	0.24
Si	0	0.050	0.55

Figure S6: XRR measurement and fit of Si/native SiO_2/ HfO_2 (plasma-assisted ALD, 200°C).

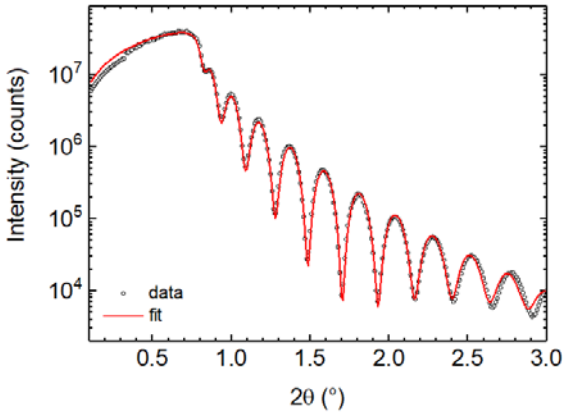

material	thickness [nm]	density [atoms/Å^3]	roughness [nm]
HfO_2	34.9	0.027	1.0
SiO_2 (native oxide)	1.9	0.023	0.24
Si	0	0.050	0.55

Figure S7: XRR measurement and fit of Si/native SiO_2/ HfO_2 (plasma-assisted ALD, 300°C).

Section S3: Supplementary information for the PDF analysis of sample type (i) PZT on Pt

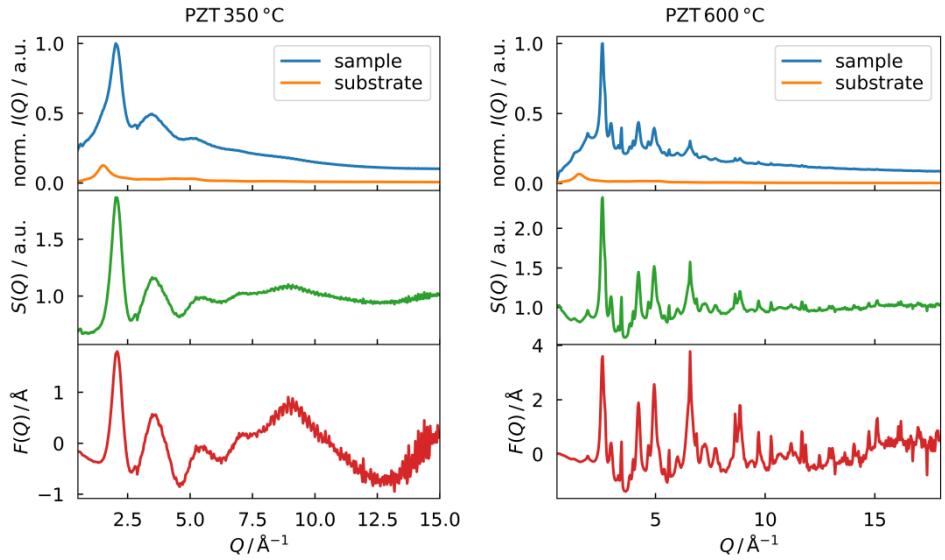

Figure S8: *I(Q)* of sample and scaled *I(Q)* of substrate, resulting S*(Q)*, and *F(Q)* for the PZT on Pt samples. The *Q* axis is scaled to the respective Q_{max} used for the Fourier transform into the PDF.

Table S3: References for PZT and related phases from the ICSD database.

composition	crystal symmetry	space group	ICSD reference code
$Pb(Zr_{0.53}Zr_{0.47})O_3$	rhombohedral	$R3m$	90700
$Pb(Zr_{0.52}Zr_{0.48})O_3$	cubic	$Pm\bar{3}m$	153401
	tetragonal	$P4mm$	90478
	monoclinic	Cm	51705
PbO	orthorhombic	$Pbcm$	40180
	tetragonal	$P4/nmm$	15466
ZrO_2	monoclinic	$P2_1/c$	658755

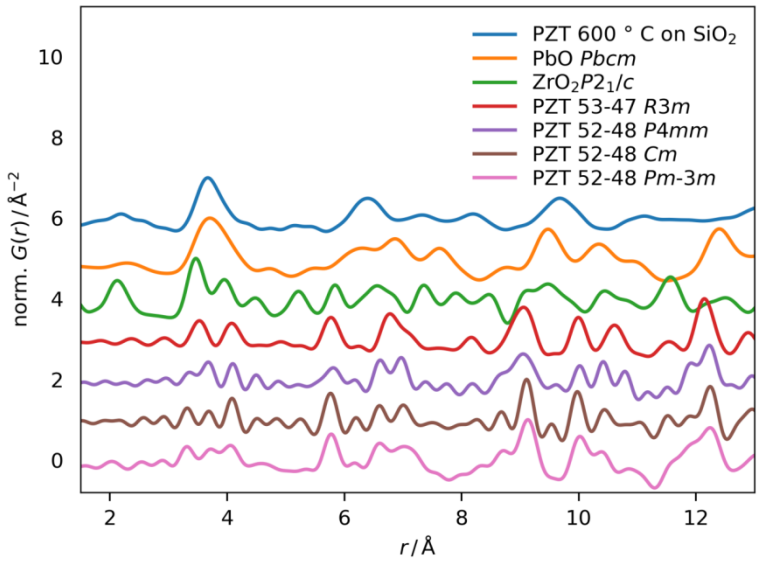

Figure S9: PDF obtained for a PZT layer deposited directly on fused silica and annealed at 600 °C, with PDFs calculated for reference phases for PZT, PbO, and ZrO_2.

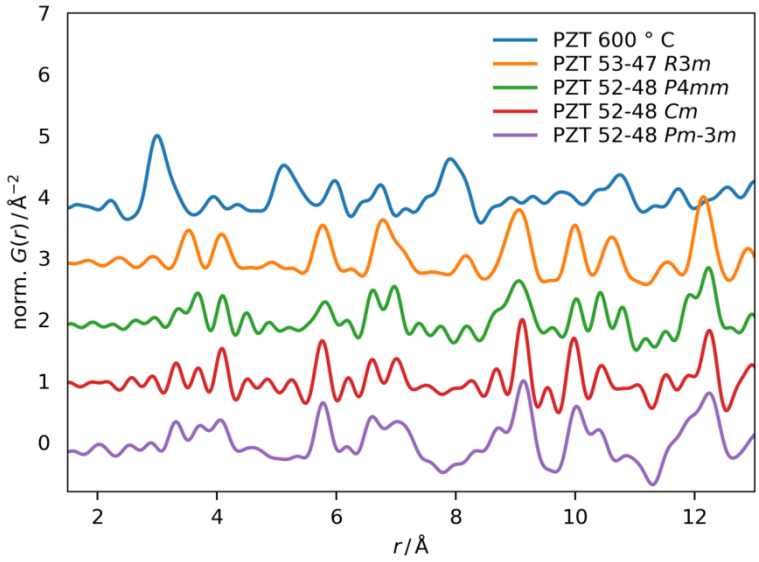

Figure S10: PDF obtained for a PZT layer deposited on Pt and annealed at 600 °C, with PDFs calculated for different reference phases for PZT of similar compositions as indicated.

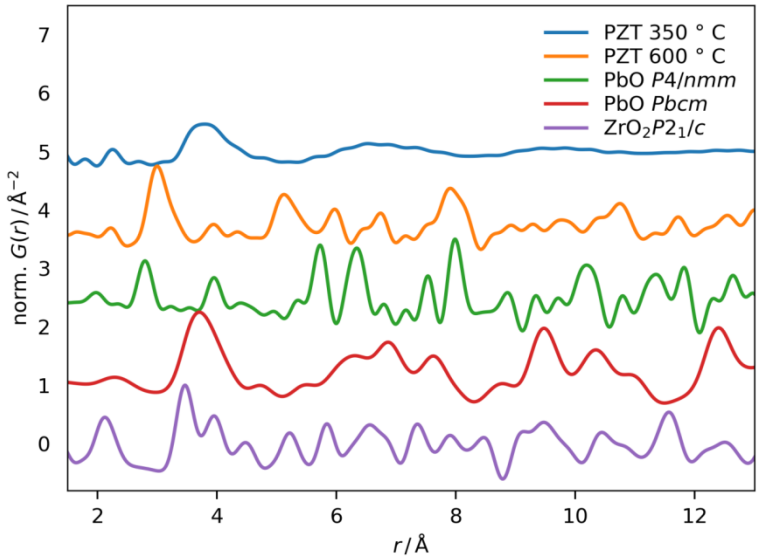

Figure S11: PDFs obtained for the PZT layers deposited on Pt and annealed at 350 °C and 600 °C, with calculated PDFs for reference phases of PbO and ZrO_2.

Section S4: Supplementary information for the PDF analysis of sample type (ii) HfO_2 on TiN and sample type (iii) TiO_x on HfO_2

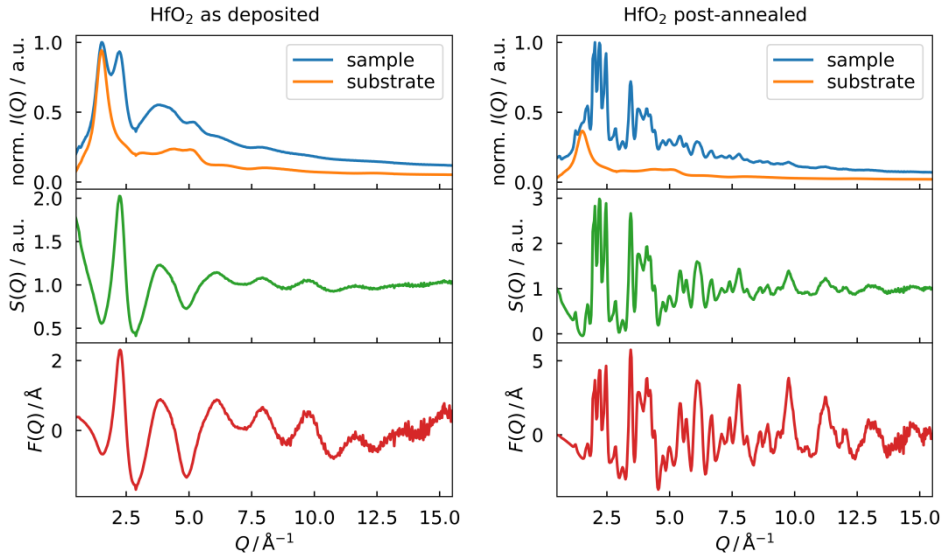

Figure S12: *I(Q)* of sample and scaled *I(Q)* of substrate, resulting S*(Q)*, and *F(Q)* for the HfO_2 on TiN bilayers as representative datasets for disordered and crystallised HfO_2 films of samples type (ii) and (iii). The *Q* axis is scaled to the respective Q_{max} used for the Fourier transform into the PDF.

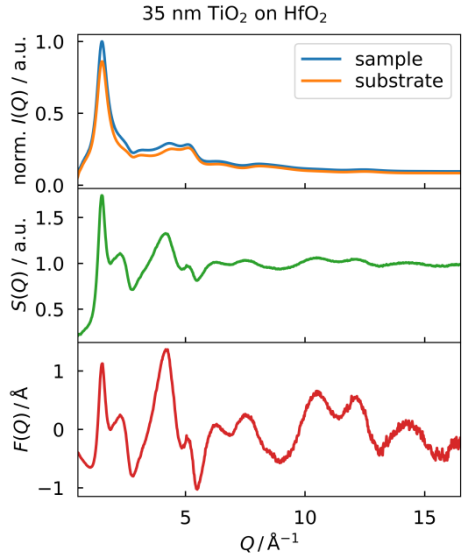

Figure S13: *I(Q)* of sample and scaled *I(Q)* of substrate, resulting S*(Q)*, and *F(Q)* for the TiO_x on HfO_2 as a representative dataset for the disordered TiO_x films of samples type (iii). The *Q* axis is scaled to the Q_{max} used for the Fourier transform into the PDF.

Table S4: References for the HfO_2 phases from the ICSD database.

composition	crystal symmetry	space group	ICSD reference code
HfO_2	monocliniic	$P2_1/c$	27313
	tetragonal	$P4_2/nmc$	173966

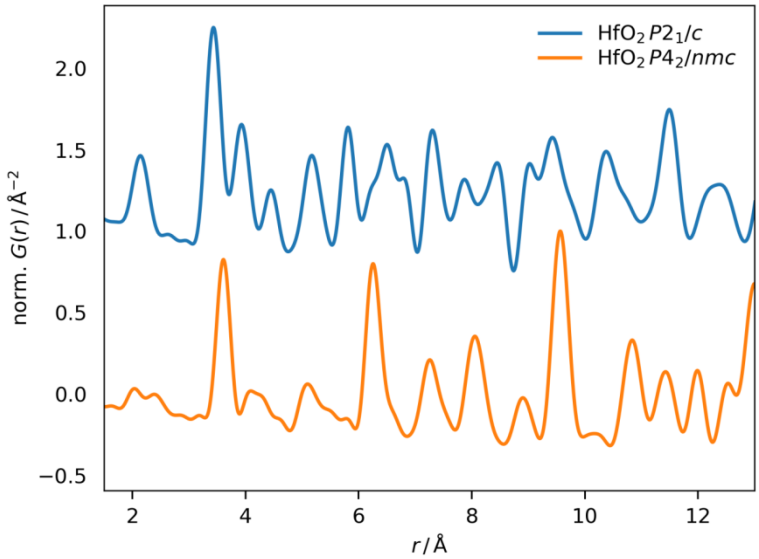

Figure S14: Calculated PDFs for selected HfO_2 phases.

Table S5. Parameters of the PDFgui refinements for the HfO_2 films described in Sections 3.2 (shown in Figure 3b) and Section 3.3 (shown in Figure 5b). For comparison, the corresponding values for the reference data are given. Since uncertainties were not propagated in the data processing, the given uncertainties are not reliable and quoted here for rough comparison only. Parameters m1-9 are defined in Table S6.

parameter	sputter deposited HfO_2 post-annealed	ALD-HfO_2 300 °C post-annealed	monoclinic HfO_2 space group $P2_1/c$
a / Å	5.1658 (0.0071)	5.1381 (0.0091)	5.1126
b / Å	5.2057 (0.0064)	5.1665 (0.0094)	5.1722
c / Å	5.3524 (0.0061)	5.3197 (0.0083)	5.2948
β / °	99.10 (0.11)	99.17 (0.15)	99.18
scale factor	0.685 (0.026)	0.184 (0.019)	
m1	0.2755 (0.0011)	0.2744 (0.0023)	0.2759
m2	0.4643 (0.0012)	0.462 (0.002)	0.4588
m3	0.7080 (0.0015)	0.7063 (0.0026)	0.7078
m4	0.074 (0.023)	0.105 (0.024)	0.073
m5	0.211 (0.018)	0.158 (0.021)	0.154
m6	0.848 (0.029)	0.824 (0.023)	0.832
m7	0.380 (0.032)	0.456 (0.022)	0.446
m8	0.799 (0.024)	0.768 (0.024)	0.752
m9	0.93 (0.02)	0.950 (0.018)	0.988
U_{iso} (Hf)	0.0086 (0.0006)	0.00400 (0.00083)	0.00569932
U_{iso} (O)	0.050 (0.022)	0.0095 (0.0084)	0.00569932
δ_2	3.52 (0.59)	3.7 (3.8)	
spherical particle diameter / Å	56.2 (3.4)	102 (30)	
refinement range / Å	1.5-60	1.5-100	
R_w	23 %	40 %	

Table S6. Refinement parameters for atomic coordinates based on symmetry constraints for the monoclinic phase, space group $P2_1/c$, as listed in Table S5.

site	*x*	*y*	*z*
Hf1	m1	m2	m3
Hf2	-m1 + 1	m2 + 0.5	-m3 + 1.5
Hf3	-m1 + 1	-m2 + 1	-m3 + 1
Hf4	m1	-m2 + 0.5	m3 – 0.5
O1	m4	m5	m6
O2	-m4 + 1	m5 + 0.5	-m6 + 1.5
O3	-m4 + 1	-m5 + 1	-m6 + 1
O4	m4	-m5 + 0.5	m6 – 0.5
O5	m7	m8	m9
O6	-m7 + 1	m8 - 0.5	-m9 + 1.5
O7	-m7 + 1	-m8 + 1	-m9 + 1
O8	m7	-m8 + 1.5	m9 – 0.5

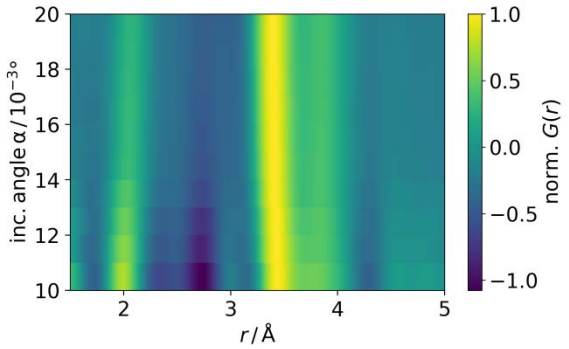

Figure S15: PDFs of the as-deposited TiO_x on HfO_2 (ALD, 300 °C) bilayer in dependence on the incidence angle α.

Table S7: References for the TiO_x phases from the ICSD database.

composition	crystal symmetry	space group	ICSD reference code
TiO	hexagonal	$P\bar{6}2m$	196273
	monoclinic	$A2/m$	15327
TiO_2 (anatase)	tetragonal	$I4_1/amd$	9852
TiO_2 (brookite)	orthorhombic	$Pbca$	36408
TiO_2 (rutile)	tetragonal	$P4_2/mnm$	9161
Ti_2O_3 (corundum)	rhombohedral	$R\bar{3}c$	1462
Ti_3O_5	monoclinic	$C2/m$	26492
	orthorhombic	$Cmcm$	50984
	orthorhombic	$I2/c$	35148
	orthorhombic	$P2/a$	194465
Ti_4O_7	triclinic	$A\bar{1}$	10148
Ti_5O_9	triclinic	$P\bar{1}$	9038
	triclinic	$P1$	653560
Ti_6O_{11}	monoclinic	$C2/m$	90958
	triclinic	$P\bar{1}$	35121
Ti_7O_{13}	triclinic	$I\bar{1}$	35122
Ti_8O_{15}	triclinic	$I\bar{1}$	35123
Ti_9O_{17}	triclinic	$P\bar{1}$	9042

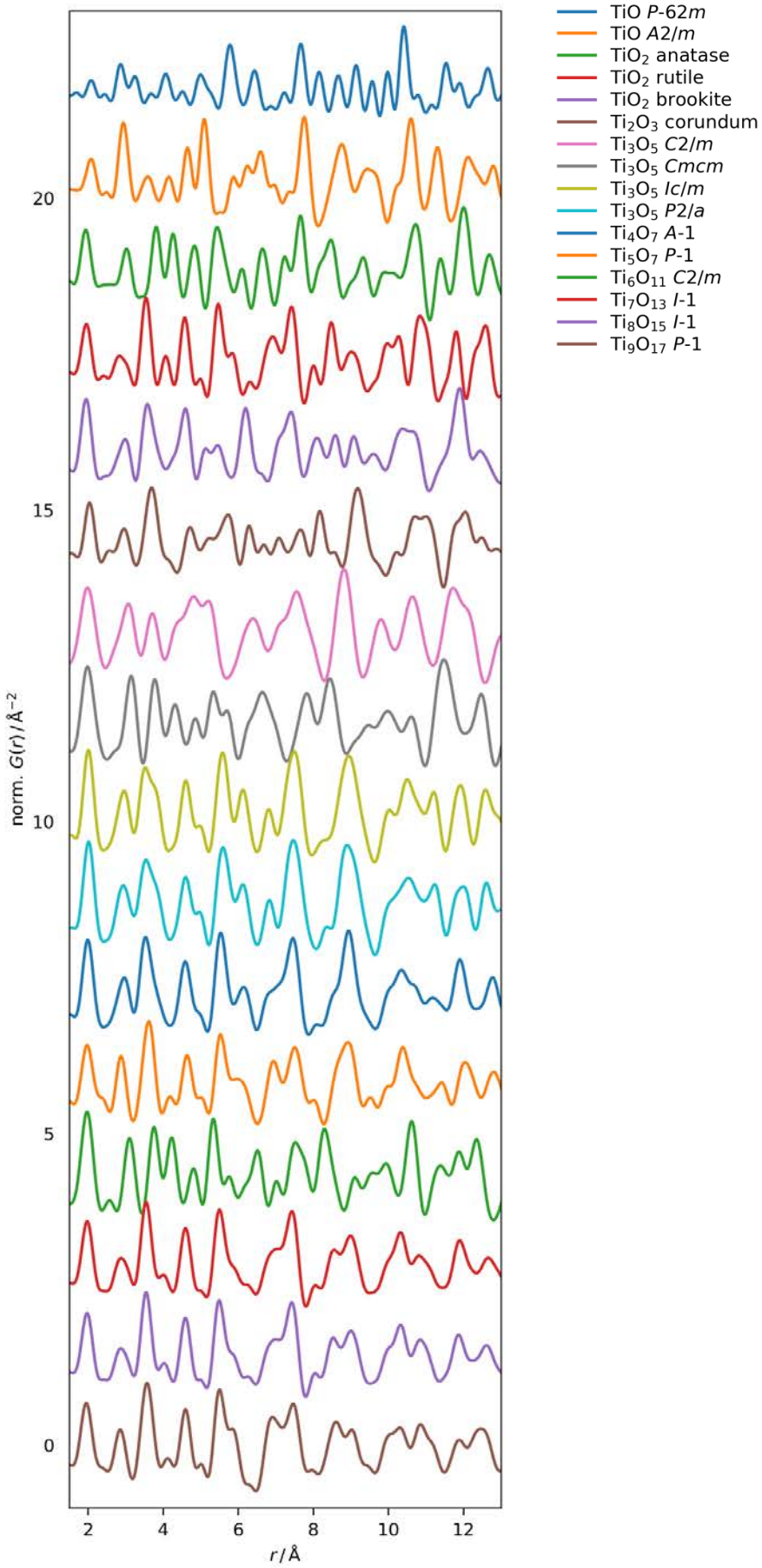

Figure S16: Calculated PDFs for different Ti_nO_{2n-1} phases for the range $1 \leq n \leq 9$.